Wide field adaptive optics laboratory demonstration with closed-loop tomographic control

Anne Costille, Cyril Petit, Jean-Marc Conan, Caroline Kulcsár, Henri-François Raynaud, Thierry Fusco

Wide Field Adaptive Optics laboratory demonstration with closed-loop tomographic control

Anne Costille[1,*], Cyril Petit[1], Jean-Marc Conan[1], Caroline Kulcsár[2], Henri-François Raynaud[2] and Thierry Fusco[1]

[1] *ONERA, DOTA-HRA*

BP72 29 avenue de la division Leclerc

92322 Chatillon Cedex, France

[2] *L2TI laboratory, University Paris 13*

93430 Villetaneuse, France

[*] *Corresponding author: cyril.petit@onera.fr*

HOMER bench, the new bench developed at ONERA devoted to wide field adaptive optics (WFAO) laboratory research, has allowed the first experimental validations of multi-conjugate adaptive optics (MCAO) and laser tomography adaptive optics (LTAO) concepts with a linear quadratic Gaussian (LQG) control approach. Results obtained in LTAO in closed loop show the significant gain in performance brought by LQG control, ***which allows tomographic reconstruction***. We present ***a*** calibration and model identification strategy. Experimental results are shown to be consistent with end-to-end simulations. These results are very encouraging and demonstrate a certain robustness of performance with respect to inevitable experimental uncertainties. These results represent a first step for the study of very large telescopes (VLT) and extremely large telescopes (ELT) instruments.

OCIS codes: 010.1080,010.1285,100.3190,170.6960

1. Introduction

Classic adaptive optics (AO) [1] is now a proven technique to correct turbulence on earth based astronomical telescopes. The corrected field of view (FoV) is however limited by the anisoplanatism effect. Multi-conjugate AO (MCAO) [2–4] aims at providing a wide FoV correction through the use of several deformable mirrors (DMs) and of ***multiple guide stars (GSs) and wavefront sensors (WFS)***. The light coming from the GSs is analyzed and **is** used to perform a tomographic reconstruction of atmospheric turbulence. The correction is made with several DMs conjugated with different altitudes. Various related concepts, such as ground layer AO (GLAO) [4, 5], laser tomographic AO (LTAO) [6] or multi-object AO (MOAO) [7] have been proposed to increase the FoV. These concepts of wide field AO (WFAO) systems are investigated for the development of **the** second generation instruments for very large telescopes (VLT) and **the first generation instruments for extremely large telescopes (ELT)**.

This paper proposes a study of these various WFAO concepts on a laboratory bench. We implement and compare these approaches in closed-loop and evaluate their performance. We also focus on calibration and control issues for WFAO systems. Contrary to AO, these systems indeed require the specification of a FoV where the correction has to be optimized and thus involve tomographic reconstruction and correction. Classic control laws with an integrator control, similar to the ones used in an AO configuration, cannot provide easily an optimal correction in a given FoV. Thus, new approaches for reconstruction and control have been developed for WFAO. Optimal tomographic reconstruction is well known in a static configuration, the solution being provided by a minimum mean square error (MMSE) estimator [8, 9]. But, this solution is not adapted to closed-loop with turbulence dynamics. The Linear Quadratic Gaussian (LQG) approach has been proposed for AO systems starting in the early 90's [10–13]. In [14, 15], it was shown that a discrete-time LQG control based on temporal averaged variables resulted in optimal performance of AO and WFAO systems (in the sense of minimum residual phase variance or maximum Strehl Ratio (SR)). This approach

has been studied in WFAO in [16]. In this paper, we focus on ***a*** comparison between integrator and LQG control in WFAO with strong emphasis on experimental validations. Comparisons with other sub-optimal solutions (e.g. POLC [17–19], FrIM [20]...) are beyond the scope of this paper.

The design of instruments for these new WFAO concepts is in progress but until now, few WFAO systems have been implemented to test calibration, performance and control issues. The ESO demonstrator MAD has proven the feasibility of GLAO and MCAO and has given the first on-sky results for these configurations using **an** integrator control [21, 22] on the VLT in Chile. Other few on-sky experiments [23] have been performed on the 6.5m MMT telescope in Arizona to evaluate tomographic reconstruction in static mode; no correction by a DM is considered and the time evolution of turbulence is not accounted for. Concerning instruments, the Gemini MCAO project is under study and integration, and will be the first MCAO on-sky instrument for an 8 meter class telescope [24]. Few laboratory test benches have been developed in parallel. **The pseudo-open loop control (POLC) approach** has been experimentally demonstrated on few closed-loop iterations [25] on the Lick Observatory Laboratory for **adaptive optics** multiconjugate testbed. This bench has also been used to test tomographic reconstruction in LTAO in an open-loop configuration [26]. No temporal aspects are considered for these results. **The ESO demonstrator MAD** has also given results in ***the*** laboratory in MCAO. Validation of LQG control in AO has been realized through laboratory experiments in AO [27, 28] and in a simplified WFAO configuration [29]. There is thus a need for the development of laboratory benches to test in closed-loop conditions GLAO, LTAO and MCAO. One also needs to define WFAO control strategies and to compare experimentally LQG control with other solutions.

In this context, we have developed a WFAO bench at ONERA, called HOMER (Hartmann oriented multi-conjugated experimental resource) dedicated to laboratory research for the demonstration and the study of new WFAO concepts, especially GLAO, LTAO and MCAO. All WFS GSs in HOMER are natural ones so that we refer in the following to the TAO

concept: it is the same concept as LTAO but implemented with natural GSs. We present here an experimental demonstration of MCAO and the first experimental results obtained in TAO configuration in closed-loop. For the first time, **a** LQG control is used in WFAO. We study the implementation of MCAO and TAO concepts on the experimental bench HOMER in terms of control and calibration aspects. We show the gain in performance brought by using **a** LQG control, especially in a TAO case, that allows tomographic reconstruction and correction in real time with a closed-loop system.

Section 2 describes HOMER bench and its main components. We define the framework of our study, the turbulence conditions and the different configurations available on the bench. **Section 3 is focused** on the formalism of WFAO and the description of the control laws applied on the bench. We recall the main equations of **the** integrator control for each configuration (Subsection 3.B) and **the** LQG optimal control solution (Subsection 3.C). In particular, we describe our approach of LQG control in the DM space. Note that DM's dynamics can be neglected since the mirrors' time constants are very small compared to integration time (see e.g. [30, 31] for AO control with DMs' dynamics). **In** section 4, we present experimental results obtained on HOMER bench. We focus on calibration aspects related to WFAO systems and on **the** implementation of control laws, with a special attention to model identification for **the** LQG control (Subsection 4.A). We present AO performance results on HOMER with an integrator control, and show the impact of the anisoplanatism effect (Subsection 4.B). Then we implement ***an*** LQG control law in ***a*** MCAO configuration (Subsection 4.C) and compare the performance obtained with an integrator control. We also compare experimental with numerical results obtained with end-to-end simulations of HOMER bench and we discuss the sensitivity to parameters tuning. Finally, we describe in Subsection 4.D the first results obtained in a TAO configuration in closed-loop, and we compare the performance of LQG control with the performance in AO in the same direction. We implement GLAO with an integrator control and show the performance of this concept. These results are also ***compared*** to numerical simulations.

2. HOMER bench

HOMER is a WFAO laboratory bench in visible wavelengths. It is devoted to implementation and validation of new concepts of WFAO in the perspective of future VLT/ELT AO systems. We can address with this bench experimental studies of implementation and comparison of control laws. We can also study calibration issues: impact and correction of field aberrations and calibration of models for control implementation.

In this paper, we test different concepts of WFAO: MCAO, TAO and GLAO. All concepts have in common the use of several WFS GSs to analyze the turbulent volume. MCAO provides a correction optimized in the whole FoV thanks to several DMs. In our configuration, two DMs are used: one conjugated with the entrance pupil, the other in altitude. We also implement TAO and GLAO concepts that use a single DM conjugated with the entrance pupil to correct the turbulence. The main difference between these two configurations is their purpose: GLAO provides a uniform but low quality correction in a wide FoV (typically 5 arcmin). On the contrary, TAO optimizes the correction in a single direction of the FoV. Correction quality is high but of course restricted to a few anisoplanatic patch (few arcseconds as in AO). It allows ***compensation*** in a direction where there is no bright GS for wavefront (WF) sensing. This configuration requires a tomographic reconstruction of the turbulent volume to estimate and to correct in the direction of interest. We study in Section 4 the implementation of these concepts on HOMER with different control laws.

In the following, we describe HOMER and its main components, represented on Fig. 1 (more details about HOMER and its components can be find on HOMER web site: www.onera.fr/dota/homer). The bench has been integrated since October 2007. It uses only natural GSs. The source module is based on a reconfigurable multi-source system composed of fiber coupled laser diodes in the visible wavelengths ($\lambda = 635 \pm 5$ nm) and associated to a collimator. Then, there is a turbulent space where phase screens could be placed to generate the turbulence. In our experiment, we use the two DMs both to generate and **to** correct **the** turbulence, as described in Subsection 2.B. This configuration **provides a more**

controlled environment and presents interesting features for control laws validations. A single wide field Shack-Hartmann WFS analyzes the light coming from several GSs. This single WFS allows ***flexibility in*** the number and **the** configuration of GSs, while reducing the calibration and synchronization issues. See Subsection 2.C for more details. A wide field imaging camera is used for performance estimation. The WFAO loops are controlled by a real time computer (RTC) working at 10 Hz (limited by WFS images time transfer).

The pattern of science targets and GSs is represented on Fig. 2. Thirteen point sources are distributed over the FoV to evaluate the performance of **the** WFAO systems. Star number 0 is in the center of the FoV and **is** used for AO WFS. For WFAO configurations, we analyze the light coming from stars 3, 6 and 10. We identify a given star in the FoV by its angular position with respect to the central star 0. The position can also be expressed in relative separation δ at a given altitude h: $\delta = \alpha h/D$ where α is the angular position of the star and D is the pupil diameter. It corresponds to the relative separation of the beam footprints at this altitude. In the following, the position of the second DM sets the FoV to $\delta = [-0.34, 0.34]$ for stars number 3, 6, 9 and 12. By analogy, if we consider a telescope with $D = 8$ m and two stars separated by 1 arcmin, a footprint relative separation of 0.34 is obtained for a turbulent layer at 9347 meters. Figure 3 **illustrates** the relative separation for two stars in the FoV for a layer at altitude h.

2.A. Corrective optics

The corrective system of HOMER is composed of two DMs, developed by ALPAO and based on magnetic actuators: a continuous membrane is deformed by miniaturized voice-coil actuators. There is no contact between the membrane and the coil array. The ground DM, called DM52, has 52 effective actuators in a 17.5 mm pupil (8x8 actuator grid). The altitude DM, called DM88, has 88 effective actuators on a 22.5 mm diameter (10x10 actuator grid). See a picture of the DMs on figure 1. Note that these DMs have an important coupling factor between their actuators (70% for DM52 and 65% for DM88). In the following, we modeled

the DMs by their influence functions that relate the DM command voltages to the correction phase expressed in a given basis. These influence functions, denoted as $\mathbf{N}^{52}$ and $\mathbf{N}^{88}$ for both DMs, are deduced from experimental calibrations. At the considered sampling frequency, DM temporal response can be considered instantaneous. We assume that the DMs are linear so that the correction phase φ^k provided by one DM k, where k stands for 52 or 88, is given by

$$\varphi^k = \mathbf{N}^k \mathbf{u}^k, \tag{1}$$

where $\mathbf{u}^k$ is the voltage vector applied on DM k. Thus, the best DM least-square fit to a given phase φ^k is obtained with the computation of voltages $\mathbf{u}^k$ through

$$\mathbf{u}^k = \mathbf{P}^k \varphi^k = ((\mathbf{N}^k)^{\mathrm{t}} \mathbf{N}^k)^{\dagger} (\mathbf{N}^k)^{\mathrm{t}} \varphi^k, \tag{2}$$

where $\mathbf{P}^k$ is the projection matrix on the DM, defined as the generalized inverse of the influence matrix $\mathbf{N}^k$ computed using a truncated singular value decomposition (TSVD). Symbol † corresponds to generalized inverse and $^{\mathrm{t}}$ stands for transposition. We thus note $\mathbf{P}^{52}$ and $\mathbf{P}^{88}$ the projection matrices of DM52 and DM88.

The DM88 can be placed at an adjustable altitude. Usually, it is placed within a collimated beam: the meta-pupil increases with the altitude, while the footprint associated to each GS keeps its size. Our configuration is a "constant envelope collimation" [32]. The DM88 is placed within a diverging beam so that the size of the meta-pupil is constant and can be set to the DM diameter, while the size of the GS footprint decreases when the altitude increases. Therefore the altitude of the second DM is continuously adjustable thanks to a simple translation stage. Figure 4 presents the optical layout of a constant envelope collimator. In the following, we conjugate the DM88 with an altitude that ensures a footprint maximum relative separation with respect to the central star of $\delta = 0.34$ for stars number 3, 6, 9 and 12 **on Fig. 2**.

2.B. *Turbulence generator*

In our experiment, the turbulence is generated by the DMs thanks to DMs voltages also called in this paper "turbulent voltages" and denoted as $\mathbf{v}$. At each step of the loop, the turbulent voltages, which are not known by the control loop, are added to the command voltages calculated by the control law. To have a realistic turbulent phenomenon, we project on the DMs a two layer Kolmogorov turbulence in translation (Taylor hypothesis) defined as two large phase screens of typically 4096×4096 pixels. The turbulence is then defined as a circular footprint of 119×119 pixels in the pupil layer and of 234×234 pixels in the altitude layer. We scale the turbulence so as to obtain an equivalent strength in each layer, a global D/r_0 equals to 7 at 635 nm. The simulated wind speed in each layer V is scaled to reproduce a ratio $V/(DF_s)$ similar to a VLT case ($V/D = 1$ Hz in each layer at $F_s = 500$ Hz). At each time step (one frame period corresponding to the $F_s = 10$ Hz frequency of the bench), the turbulent phase in each layer φ^k, where k stands for 52 and 88, is translated and projected on the DM corresponding to its altitude according to Eq. (2) to compute the DM voltages $\mathbf{v}^k$. We can assume that the turbulent phase is a stationary Gaussian process with known covariance matrix Σ_φ^k derived from Kolmogorov statistics [33] on the Zernike basis. For each turbulent voltage $\mathbf{v}^k$ corresponding to a layer, the voltages covariance matrix denoted by $\Sigma_\mathbf{v}^k$ is obtained through

$$\Sigma_\mathbf{v}^k = \mathbf{P}^k \Sigma_\varphi^k (\mathbf{P}^k)^\mathrm{t}. \tag{3}$$

This configuration allows us to benefit from a well controlled and calibrated turbulent environment. The turbulent phase being in the DM space, we simply have to be aware of the fact that there is a limited aliasing effect and virtually no fitting error.

2.C. *Wavefront sensors*

The WFS is a wide field Shack-Hartmann composed of a 7x7 sub-aperture lenslet array (1.136 mm pitch, 30 mm focal length) and an ANDOR iXon DU895LC camera, which is a low noise EMCCD with 1004x1002 pixels of 8 microns. The large number of pixels of the

camera imposes a low acquisition frequency of 24 Hz at most. Each lens focuses the GS's lights on the WFS camera detector over 142x142 pixels ($\lambda/2D$ per pixel, Shannon sampling). Note that its FoV is slightly lower than the source FoV. A distinctive feature of HOMER design is that a single wide field Shack-Hartmann WFS is used instead of having a given number of WFS for each GS direction: each sub-aperture can see the whole FoV. We can then perform WF sensing on several regions, of 16×16 pixels for instance, around each selected GS. It allows to test different WFS configurations with minimal hardware alteration, to simplify **the** calibration procedure and to ensure **the** synchronization of the measurements. See a picture of the WFS on Fig. 1 and its display on Fig. 5.

2.D. Real-time computer

The HOMER RTC has been developed by Shaktiware based on **the** specifications provided by ONERA. We use a PC under linux-64 bits operating system, with an AMD K8 Athlon 64 processor. It is based on a C code which allows an easy use of the software. The RTC integrates various specificities for WFS: multi-zone WFS with slope computation through either center of gravity, weighted center of gravity or even a correlation algorithm. **Several kinds of control laws can be easily implement on the RTC, such as integrator or LQG control**. The RTC presents many functionalities that allow implementation and diagnostic tools for WFAO loops.

3. WFAO system and control formalism

3.A. WFAO formalism

This section describes the formalism and the modeling of **a** WFAO system. Figure 6 **shows** a general WFAO configuration using n_m DMs for correction and n_{gs} WFS for analysis. There is a two frame delay in the system: WFS measurements are performed during one frame of length T, then CCD read-out, slopes calculation and control computation are performed during the next frame. Control is applied at the beginning of the frame after. It leads to the

chronogram presented on Fig. 7. More complex chronograms can be considered [28, 30, 34].

It is assumed that the atmosphere can be modeled by n_ℓ discrete turbulent layers statistically independent. Each layer ℓ is characterized by its altitude h_ℓ. $\varphi^{tur}_{\ell,n}$ is the time-averaged turbulent phase at time nT in the layer ℓ, corresponding to the discrete instant n:

$$\varphi^{tur}_{\ell,n} = \frac{1}{T}\int_{(n-1)T}^{nT} \varphi^{tur}_{\ell}(t)dt. \tag{4}$$

It is defined over a meta-pupil delimited by the maximal FoV, the diameter of which is $D_\ell = D + h_\ell\theta$. The turbulence can be expanded on a convenient modal basis. In the following, we choose the DM space to represent the turbulent phase, instead of the usual Zernike basis, as the turbulence is generated by the DMs (see Subsection 3.C for more details).

The turbulent phase in the volume φ^{tur}_n is defined by the concatenation of the turbulent phases in each layer ℓ. For a WFAO system with several WFS directions $\alpha = \{\alpha_0, ..., \alpha_{n_{gs}}\}$, the turbulent phase seen in the telescope pupil is equal to $\phi^{tur}_{\alpha,n} = \mathbf{M}^{n_\ell}_\alpha \varphi^{tur}_n$, where $\mathbf{M}^{n_\ell}_\alpha$ is a linear operator performing the sum of all contributions of each turbulent layer ℓ in all directions α. The correction phase in the n_{obj} directions of interest $\beta = \{\beta_0, ..., \beta_{n_{obj}}\}$ in the pupil is then given in a similar way by $\phi^{cor}_{\beta,n} = \mathbf{M}^{n_m}_\beta \varphi^{cor}_n$.

We consider a WFAO system composed of n_{gs} WFSs and n_m DMs, which applies a correction in n_{obj} directions of interest β. Let $\mathbf{u}_n$ be the voltage vector at instant n gathering all DM voltage vectors $\mathbf{u}_{m,n}$ ($m \in \{1, ..., n_m\}$) then $\mathbf{u}_n = ((\mathbf{u}_{1,n})^{\mathrm{t}}, ..., (\mathbf{u}_{n_m,n})^{\mathrm{t}})^{\mathrm{t}}$. We denote by $\mathbf{N}$ the DMs' global influence matrix. This is a block-diagonal matrix, each block corresponding to an influence matrix of the WFAO system's mirrors. The correction phase provided in the volume φ^{cor}_n is then defined as a generalization of Eq. (1)

$$\varphi^{cor}_n = \frac{1}{T}\int_{(n-1)T}^{nT} \varphi^{cor}(t)dt = \mathbf{N}\mathbf{u}_{n-1}. \tag{5}$$

The residual phase at time $n-1$ in directions of interest β is given by

$$\phi^{res}_{\beta,n-1} = \mathbf{M}^{n_\ell}_{\beta}\varphi^{tur}_{n-1} - \mathbf{M}^{n_m}_{\beta}\varphi^{cor}_{n-1}. \tag{6}$$

The residual WFS measurements, obtained thanks to n_{gs} WFSs in directions of analysis α, are

$$\mathbf{y}_n = \mathbf{D}_{n_{gs}}\phi^{res}_{\alpha,n-1} + \mathbf{w}_n, \tag{7}$$

where $\mathbf{D}_{n_{gs}}$ contains n_{gs} row repetition of matrix $\mathbf{D}$, which describes the linear response of a WFS and assuming that all WFSs are identical. The measurement noise $\mathbf{w}_n$ is a generalized measurement noise vector for all WFSs. In the following, we call the WFAO interaction matrix $\mathbf{M}^{n_{gs},n_m}_{int}$ the matrix that relays the slopes measurements to the voltages applied on the DM

$$\mathbf{y}_n = -\mathbf{M}^{n_{gs},n_m}_{int}\mathbf{u}_n = -\mathbf{D}_{n_{gs}}\mathbf{M}^{n_m}_{\alpha}\mathbf{N}\mathbf{u}_n. \tag{8}$$

A classic AO configuration is easily retrieved, by setting $\mathbf{M}^{n_\ell}_{\alpha}$,$\mathbf{M}^{n_m}_{\alpha}$,$\mathbf{M}^{n_m}_{\beta}$ and $\mathbf{M}^{n_\ell}_{\beta}$ as identity matrices and considering single WFS, DM and on-axis analysis and correction direction.

The WFAO performance optimality criterion aims at minimizing the residual phase variance in a given FoV, hence the minimization of the following criterion

$$\mathbf{J}(\mathbf{u})^{wfao} = \lim_{N\to+\infty}\frac{1}{N}\sum_{n=1}^{N}\left\|\mathbf{M}^{n_\ell}_{\beta}\varphi^{tur}_{n} - \mathbf{M}^{n_m}_{\beta}\mathbf{N}\mathbf{u}_{n-1}\right\|^2. \tag{9}$$

3.B. Integrator control

what we call in the following the integrator control implemented on HOMER for different WFAO configurations. This control does not minimize the criterion presented on Eq. (9) but **it** corresponds to a least-square reconstructor associated with an integrator temporal control. The control applied at time nT is described by

$$\mathbf{u}_n = \mathbf{u}_{n-1} + g\Delta\mathbf{u}^{ls}_n = \mathbf{u}_{n-1} + g\mathbf{M}_{com}\mathbf{y}_n, \tag{10}$$

where g is the integrator scalar gain, $\mathbf{M}_{com}$ is the control matrix of the loop and $\mathbf{y}_n$ is the WFS measurements of the residual phase in n_{gs} directions. Voltage increments $\Delta\mathbf{u}_n^{ls}$ are computed from the closed-loop WFS data by least-square reconstruction. We describe here the different control matrices used for:

- AO loop: $\mathbf{M}_{com}^{ao} = ((\mathbf{M}_{int}^{ao})^{\mathrm{t}}\mathbf{M}_{int}^{ao})^{\dagger}(\mathbf{M}_{int}^{ao})^{\mathrm{t}}$ is the generalized inverse of the interaction matrix $\mathbf{M}_{int}^{ao} = \mathbf{DN}$ using a TSVD. Note that in this configuration $n_{gs} = 1$ and $n_m = 1$ so that $\mathbf{M}_{\alpha}^{n_m}$ in Eq. (8) is equal to identity matrix and $\mathbf{N} = \mathbf{N}^{52}$,

- GLAO loop: $\mathbf{M}_{com}^{glao} = ((\mathbf{M}_{int}^{glao})^{\mathrm{t}}\mathbf{M}_{int}^{glao})^{\dagger}(\mathbf{M}_{int}^{glao})^{\mathrm{t}}$ makes an average of the measurements in n_{gs} directions and applies the correction on $n_m = 1$ DM with $\mathbf{M}_{int}^{glao} = \mathbf{D}_{n_{gs}}\mathbf{N}^{52}$. The effect produced is an optimization and a standardization of the SR in a large FoV thanks to the analysis on a finite number of GSs,

- MCAO loop : $\mathbf{M}_{com}^{mcao} = ((\mathbf{M}_{int}^{mcao})^{\mathrm{t}}\mathbf{M}_{int}^{mcao})^{\dagger}(\mathbf{M}_{int}^{mcao})^{\mathrm{t}}$ where $\mathbf{M}_{int}^{mcao} = \mathbf{D}_{n_{gs}}\mathbf{M}_{\alpha}^{n_m}\mathbf{N}$ is the generalized interaction matrix of the system between the n_m DMs and the n_{gs} WFSs. The control matrix is computed using a TSVD.

The integrator control is based on the tacit hypothesis that the turbulent phase belongs to the DM space. Table 1 recalls the size of the interaction matrices for each configuration tested on HOMER. In the following, we refer to the interaction matrices with the appropriated number of DMs and WFSs so that: $\mathbf{M}_{int}^{ao} = \mathbf{M}_{int}^{1,1}$, $\mathbf{M}_{int}^{glao} = \mathbf{M}_{int}^{n_{gs},1}$ and $\mathbf{M}_{int}^{mcao} = \mathbf{M}_{int}^{n_{gs},n_m}$. For each test with **an** integrator control, we adjust the scalar gain and the number of truncated modes in the TSVD to optimize **the** integrator control performance (see Subsection 4.C.3 for more details). We work in high signal to noise (SNR) conditions. We choose the integrator gain equal to $g = 0.5$.

3.C. LQG control formalism

This part just recalls the main equations and important characteristics of **the** LQG control that has been fully described, especially in [29]. The control problem in Eq. (9) finds its

solution in a two step resolution. This classic result is known as the stochastic separation theorem [35,36] and states that the optimal control $\mathbf{u}_n$ can be constructed by separately solving a deterministic control problem and a stochastic minimum variance estimation problem. The stochastic minimum variance estimation problem consists in estimating/predicting the turbulent phase. Its solution is provided, in the linear Gaussian case, by the Kalman filter. If the Gaussian assumption is released, the Kalman filter provides the best linear unbiased estimator. To describe the LQG control, a state-space representation of the system has to be specified.

As turbulence is generated by **the** DMs, like described in Subsection 2.B, a natural way is to represent the turbulence phase in the DM space [13,37,38]. We denote by $\mathbf{v}_n$ the turbulent phase on the DM influence function basis at time n, called the turbulent voltages. We assume that the turbulent phase is $\varphi_n^{tur} = \mathbf{N}^{tur}\mathbf{v}_n$, where $\mathbf{N}^{tur}$ is a block-diagonal matrix, with two blocks containing respectively $\mathbf{N}^{52}$ and $\mathbf{N}^{88}$, which correspond to the influence matrices of the DMs that generate the turbulence. Note that $\mathbf{u}_n$ are the correction voltages calculated by the controller to be applied on one or two DMs so that $\dim(\mathbf{u}_n) \leq \dim(\mathbf{v}_n)$. We use for the sake of simplicity a first order auto-regressive (AR1) model, already successfully applied in LQG control for AO and WFAO, to model the turbulent voltages stochastic process associated to the turbulent phase of the form

$$\mathbf{v}_{n+1} = \mathbf{A}^v\mathbf{v}_n + \xi_n, \tag{11}$$

where ξ_n is a white noise of covariance matrix Σ_ξ. The matrix $\mathbf{A}^v$ is a time-constant matrix. Following usual modal turbulence models [14, 29] we consider a diagonal matrix. In the considered DM basis one can even take a matrix proportional to identity since turbulent voltages exhibit a similar correlation time for all actuators. We then do not benefit from a temporal discrimination between modes, but this aspect is not very relevant on low order systems. This AR1 model of the discrete-time turbulence, as defined in Eq. (11), is simple. It is representative of the temporal decorrelation of the turbulence and does not pretend to be representative of a frozen flow turbulence. Consequently $\mathbf{A}^v = a\mathbf{I}$ where $\mathbf{I}$ denotes identity

matrix with appropriate dimensions. It is important to note that even with such a simple diagonal matrix, the AR1 model given by Eq. (11) can be tuned so as to generate a stationary signal $\mathbf{v}$ with arbitrary spatial covariance matrix. In this case, selecting matrix Σ_φ thanks to Kolmogorov statistics leads to a given spatial covariance matrix $\Sigma_{\mathbf{v}}$ of the turbulent voltages given by Eq. (3), containing contributions for both DM52 and DM88. We then calculate the spatial covariance AR1 noise matrix Σ_ξ by taking into account the conservation of the turbulence spatial correlation structure, including its global energy:

$$\Sigma_\xi = \Sigma_{\mathbf{v}} - \mathbf{A}^v \Sigma_{\mathbf{v}} (\mathbf{A}^v)^{\mathrm{t}} = (1-a^2) \begin{pmatrix} \mathbf{P}^{52} \Sigma_\varphi^{52} (\mathbf{P}^{52})^{\mathrm{t}} & 0 \\ 0 & \mathbf{P}^{88} \Sigma_\varphi^{88} (\mathbf{P}^{88})^{\mathrm{t}} \end{pmatrix}. \tag{12}$$

Equation (12) leads to a non-diagonal $\Sigma_{\mathbf{v}}$ which means that temporal interspectra are not null: it is immediately checked that this choice of Σ_ξ results for k = 52 and k = 88 in $\Sigma_{\mathbf{v}}^k = \mathbf{P}^k \Sigma_\varphi^k (\mathbf{P}^k)^{\mathrm{t}}$ in Eq. (3), so that $\mathrm{Var}(\mathbf{N}^k \mathbf{v}^k) = \mathrm{Var}(\mathbf{P}^k \varphi^k)$.

We define a state-space model with state vector

$$\mathbf{X}_n = \begin{pmatrix} \mathbf{v}_n \\ \mathbf{v}_{n-1} \\ \mathbf{u}_{n-1} \\ \mathbf{u}_{n-2} \end{pmatrix}, \tag{13}$$

which allows to describe respectively a turbulence evolution model in the DM space (11), the measurement equation (7) and the correction phase equation (5) in matrix form:

$$\mathbf{X}_{n+1} = \mathbf{A}\mathbf{X}_n + \mathbf{B}\mathbf{u}_n + \eta_n, \tag{14}$$

$$\mathbf{y}_n = \mathbf{C}\mathbf{X}_n + \mathbf{w}_n, \tag{15}$$

where

$$\mathbf{A} = \begin{pmatrix} \mathbf{A}^v & 0 & 0 & 0 \\ \mathbf{I} & 0 & 0 & 0 \\ 0 & 0 & 0 & 0 \\ 0 & 0 & \mathbf{I} & 0 \end{pmatrix}, \mathbf{B} = \begin{pmatrix} 0 \\ 0 \\ \mathbf{I} \\ 0 \end{pmatrix} \text{ and } \eta_n = \begin{pmatrix} \xi_n \\ 0 \\ 0 \\ 0 \end{pmatrix}, \tag{16}$$

$$\mathbf{C} = \begin{pmatrix} 0 & \mathbf{C}_{n_\ell} & 0 & -\mathbf{C}_{n_m} \end{pmatrix}. \tag{17}$$

with $\mathbf{C}_{n_\ell} = \mathbf{D}_{n_{gs}} \mathbf{M}_\alpha^{n_\ell} \mathbf{N}^{tur}$ and $\mathbf{C}_{n_m} = \mathbf{D}_{n_{gs}} \mathbf{M}_\alpha^{n_m} \mathbf{N}$. Covariance matrix of η_n is deduced from Σ_ξ and is denoted by Σ_η.

This state space model provides a complete input-output description of a WFAO system. The optimal control is then obtained as an orthogonal projection by

$$\mathbf{u}_n = \mathbf{P}_{wfao} \hat{\mathbf{v}}_{n+1|n}, \tag{18}$$

where $\hat{\mathbf{v}}_{n+1|n}$ is the conditional expectation of $\mathbf{v}_{n+1}$ with respect to all measurements available up to time n. $\mathbf{P}_{wfao}$ is the least-square orthogonal projector from turbulent voltages space to correction voltages space given by

$$\mathbf{P}_{wfao} = \left(\left(\mathbf{M}_\beta^{n_m} \mathbf{N} \right)^{\mathrm{t}} \mathbf{M}_\beta^{n_m} \mathbf{N} \right)^\dagger (\mathbf{M}_\beta^{n_m} \mathbf{N})^{\mathrm{t}} \mathbf{M}_\beta^{n_\ell} \mathbf{N}^{tur}, \tag{19}$$

that minimizes the deterministic criterion for $\varphi_n^{tur} = \mathbf{N}^{tur} \mathbf{v}_n$:

$$\mathbf{J}(\mathbf{u})^{wfao} = \left\| \mathbf{M}_\beta^{n_\ell} \mathbf{N}^{tur} \mathbf{v}_n - \mathbf{M}_\beta^{n_m} \mathbf{N} \mathbf{u}_{n-1} \right\|^2. \tag{20}$$

Minimizing $\mathbf{M}_\beta^{n_m} \mathbf{N} \| \mathbf{v}_n - \mathbf{u}_{n-1} \|^2$ for **a** MCAO configuration leads to minimizing Eq. (20), since $n_m = n_\ell$ and $\mathbf{N} = \mathbf{N}^{tur}$, so that $\mathbf{P}_{mcao}$ is equal to identity matrix. In TAO configuration, we have to calculate the projection matrix $\mathbf{P}_{tao}$ with Eq. (19) and appropriate matrices. The computation of the projection matrices is presented in Subsection 4.A.3.

The voltage estimate is the output of the stationary Kalman filter in the form:

$$\hat{\mathbf{v}}_{n|n} = \hat{\mathbf{v}}_{n|n-1} + a\mathbf{H}_\infty \left(\mathbf{y}_n - \hat{\mathbf{y}}_{n|n-1}\right), \tag{21}$$

$$\hat{\mathbf{v}}_{n+1|n} = a\hat{\mathbf{v}}_{n|n}, \tag{22}$$

$$\mathbf{u}_n = \mathbf{P}_{wfao}\hat{\mathbf{v}}_{n+1|n}, \tag{23}$$

where $\hat{\mathbf{y}}_{n|n-1} = \mathbf{D}_{n_{gs}}\mathbf{M}_\alpha^{n_\ell}\mathbf{N}^{tur}\hat{\mathbf{v}}_{n-1|n-1} - \mathbf{D}_{n_{gs}}\mathbf{M}_\alpha^{n_m}\mathbf{N}\mathbf{u}_{n-2}$ and matrix $\mathbf{H}_\infty$ is the asymptotic Kalman gain defined by:

$$\mathbf{H}_\infty = \begin{pmatrix} a\mathbf{H}_{opt} \\ \mathbf{H}_{opt} \\ 0 \\ 0 \end{pmatrix}, \tag{24}$$

with $\mathbf{H}_{opt} = \Sigma_\infty {\mathbf{C}_{n_\ell}}^{\mathrm{t}} \left(\mathbf{C}_{n_\ell}\Sigma_\infty\mathbf{C}_{n_\ell}^{\mathrm{t}} + \Sigma_w\right)^\dagger$ and Σ_∞ is the covariance matrix of the estimation error and the solution of the Riccati equation

$$\Sigma_\infty = a^2\Sigma_\infty + \Sigma_\xi - a^2\Sigma_\infty {\mathbf{C}_{n_\ell}}^{\mathrm{t}} \left(\mathbf{C}_{n_\ell}\Sigma_\infty {\mathbf{C}_{n_\ell}}^{\mathrm{t}} + \Sigma_w\right)^\dagger \mathbf{C}_{n_\ell}\Sigma_\infty. \tag{25}$$

Note that Eq. (25) does not depend on measurements and thus can be pre-computed off-line.

4. Experimental results on HOMER bench for WFAO configurations

This section focuses on laboratory tests of different WFAO concepts on HOMER. First, Subsection 4.A presents calibration aspects necessary to our test: impact of the field aberrations (Subsection 4.A.1) and model calibration for implementation of integrator and LQG control laws (Subsection 4.A.3). We also describe the end-to-end simulation tools of HOMER in Subsection 4.A.2. Then we present the performance obtained in classical AO with **an** integrator control (Subsection 4.B). Subsection 4.C provides performance comparison be-

tween integrator and LQG control in MCAO. This is the first experimental demonstration of LQG control for a WFAO system. At last, we present the first experimental results obtained in TAO (Subsection 4.D) in closed-loop conditions. TAO correction is obtained with LQG control. These validations are systematically compared to numerical simulations.

Turbulent conditions have been fully described in Subsection 2.B. The same conditions have been used for all experiments. Note that the error bar on SR estimation defined as the 1 σ error bar is of the order of 1% for all SR values presented in the following. So the SR given in this article are round off the percent due to the error bar of the measurement.

4.A. Calibration, end-to-end simulations and model identification

Calibration is needed, not only to implement end-to-end simulations but also to compute the control laws for WFAO systems. We first have to evaluate the performance of our system without turbulence to calibrate the internal SR of HOMER. We then describe the end-to-end numerical simulation tool of the bench that **is used to** estimate and to compare the performance of the bench with experimental results. At last, we present the model identification issues for both control laws.

4.A.1. Performance of the system without turbulence

To begin with, we need to measure the performance of the system without turbulence: the internal SR is measured in the imaging camera focal plane for each star in the FoV on long exposure images (see their positions on Fig. 2). This step gives the best SR that could be reached experimentally with our system. Measurement of the internal SR is performed in closed-loop with **an** integrator control without turbulence, as described in Subsection 3.B: in AO, the GS and corrected direction is star 0; in MCAO, the GSs are the stars 3, 6 and 10. Figure 8 presents the map of internal SR obtained in AO and MCAO. In both cases, the mean SR on the imaging field is about 56%. The best performance is obtained on star 0 with 66% and the worst on star 9 with 46% after optimization of the optical alignment. The standard deviation of the SR in the FoV is 5.8% in AO and 5.6% in MCAO. These results

allow us to evaluate the optical imaging path quality of HOMER in each configuration. The SR is not uniform in the FoV, especially in MCAO case: it means that some field aberrations of the system are not corrected. These low SR can also be due to common path aberrations with high frequency effects. Figure 8 shows the impact of the aberrations in the imaging path that are not corrected by the loop. To improve further HOMER performance, it may be possible to measure NCPA on and off axis with phase diversity method [39, 40], but accounting for NCPA in WFAO closed-loop configuration is still under study. Measurement of the internal SR also allows to scale the SR obtained in end-to-end simulations of HOMER bench, presented in Subsection 4.A.2, before comparison with experimental results. In the following, the value of the internal SR will therefore be specified for each experiment.

4.A.2. End-to-end numerical simulation of HOMER bench

So as to validate the experimental results, HOMER bench has been numerically simulated using an end-to-end IDL code, as described in [29]. We have adapted this code to HOMER configuration to take into account the specificities of our system (AO, GLAO, TAO or MCAO configurations, turbulence, DM and WFS characteristics, *etc*). We simulate the turbulence with the turbulent voltages applied on the bench. Both DMs are fully represented by their experimental influence matrices. The code simulates n_{gs} Shack-Hartmann WFSs of 7×7 lenslet array, where n_{gs} corresponds to the number of WFSs for the studied configuration. The computation of the slope measurements is then obtained by a discrete approximation of the phase gradient in a sub-aperture. The WFSs are linear and each one is represented by matrix $\mathbf{D}$. The code includes a control module with either integrator or LQG control. The SR obtained in all numerical simulations is scaled to take into account the internal SR measured in Subsection 4.A.1.

4.A.3. Model identification for WFAO control

We focus now on calibration aspects for implementation of control laws for WFAO systems. Section 3 has recalled the main equations for both control laws tested on HOMER. **An**

integrator control requires to calibrate the interaction matrices presented in Subsection 3.B. They are obtained experimentally by push-pull of each actuator of the DMs. We realize an average of the slope measurements in each GS direction to limit noise. They are easily obtained thanks to an RTC routine. **The** LQG control requires a little bit more calibration of matrices and models to reach good performance. **The** LQG control can be summed up with Eq. (21), Eq. (22) and Eq. (23). As already explained, the turbulent phase is represented in the DM space. It is more convenient here: as only interaction matrices are involved, this simplifies model identification. To implement LQG control (21 - 23), we have to identify the turbulent model described in Eq. (11) and Eq. (12), and to evaluate the matrices Σ_w, $\mathbf{C}$, $\mathbf{P}_{wfao}$ and Σ_∞. This leads to identify in the DM space:

- the turbulent model: the value of the parameter a of matrix $\mathbf{A}^v$. We calculate the temporal correlation for each turbulent voltage $\mathbf{v}$ and identify the best fit to the short term correlation at one step, so that $a = 0.995$. The values of $\Sigma_{\mathbf{v}}$ and Σ_ξ are deduced from Eq. (3) and from Eq. (12).

- The noise covariance matrix Σ_w: it is chosen diagonal and proportional to identity so that $\Sigma_w = \sigma_w^2 \mathbf{I}$. We calibrate on HOMER bench the noise variance σ_w^2 : it is measured from the slope data and is equal to 5×10^{-4} pixels^2 in the following.

- The matrix $\mathbf{C}$ described in Eq. (17): it is obtained from the multiplication of matrices $\mathbf{D}_{n_{gs}}$ (model of the WFSs), $\mathbf{M}_\alpha^{n_\ell}$ (projector of the turbulent phase seen in the WFS directions), $\mathbf{M}_\alpha^{n_m}$ (projector of the correction phase) and the influence matrices of the DMs, $\mathbf{N}$ used for correction and $\mathbf{N}^{tur}$ for generation of the turbulence. Matrices $\mathbf{D}_{n_{gs}}$, $\mathbf{M}_\alpha^{n_\ell}$ and $\mathbf{M}_\alpha^{n_m}$ can be numerically computed through the end-to-end simulation of HOMER, described in Subsection 4.A.2. Matrices $\mathbf{N}$ and $\mathbf{N}^{tur}$ are obtained with experimental calibration of the DMs. Both matrices $\mathbf{C}_{n_\ell}$ and $\mathbf{C}_{n_m}$, which correspond to interaction matrices, can be measured experimentally. $\mathbf{C}_{n_\ell}$ is the interaction matrix between the WFSs and the two DMs that generate the turbulence, corresponding to

matrix $\mathbf{M}_{int}^{n_{gs},n_m}$ with $n_l = 2$ and $\mathbf{N} = \mathbf{N}^{tur}$. $\mathbf{C}_{n_m}$ corresponds to the interaction matrix between the WFSs and the DMs used for the correction. In MCAO, we thus have $\mathbf{C}_{n_m} = \mathbf{C}_{n_\ell}$, and in TAO, $n_m = 1$ and $\mathbf{N} = \mathbf{N}^{52}$ so that $\mathbf{C}_{n_m}$ corresponds to $\mathbf{M}_{int}^{n_{gs},1}$.

- The projection matrix $\mathbf{P}_{wfao}$ of the estimated turbulent voltages on the DMs: we have already shown that in MCAO, $\mathbf{P}_{mcao} = \mathbf{I}$ (see Subsection 3.C). In TAO, $\mathbf{P}_{tao}$ has to be calculated with the appropriated matrices thanks to Eq. (19). β corresponds to star 0 and $n_m = 1$ so that $\mathbf{M}_\beta^{n_m}$ is the identity matrix and $\mathbf{N}$ corresponds to $\mathbf{N}^{52}$. Therefore, $\mathbf{P}_{tao} = \left(\mathbf{N}^{52\mathrm{t}}\mathbf{N}^{52}\right)^\dagger \mathbf{N}^{52\mathrm{t}}\mathbf{M}_\beta^{n_\ell}\mathbf{N}^{tur}$. This solution mixes numerical and experimental matrices in the LQG control and makes matrices $\mathbf{C}$ and $\mathbf{P}_{tao}$ potentially inconsistent. So as to limit model errors, it is interesting to modify the criterion in Eq. (20) by minimizing at each step the criterion $\left\|\mathbf{D}(\mathbf{M}_\beta^{n_\ell}\mathbf{N}^{tur}\mathbf{v}_n - \mathbf{M}_\beta^{n_m}\mathbf{N}^{52}\mathbf{u}_{n-1})\right\|^2$. Minimizing this criterion leads to minimizing the residual slope variance in the direction of interest β. The projector $\mathbf{P}_{tao}$ is then obtained as $\mathbf{P}_{tao} = ((\mathbf{DN}^{52})^{\mathrm{t}}\mathbf{DN}^{52})^\dagger(\mathbf{DN}^{52})^{\mathrm{t}}\mathbf{DM}_\beta^{n_\ell}\mathbf{N}^{tur}$ and can be computed with experimental interaction matrices : $\mathbf{DN}^{52}$ corresponds to $\mathbf{M}_{int}^{1,1}$ and $\mathbf{DM}_\beta^{n_\ell}\mathbf{N}^{tur}$ corresponds to an MCAO like interaction matrix in the direction β that can be easily calibrated on the bench. When using this criterion, we restrict optimality to the WFSs space in minimizing residual slopes variance instead of residual phase but we gain in terms of calibration quality.

- The asymptotic Kalman gain Σ_∞ described in Eq. (25): all parameters have been evaluated before. The value of Σ_w used in the Riccati equation is tuned to obtain the best performance. See Subsection 4.C.2 for more details.

As shown in this subsection, both integrator and LQG control laws need the calibration of given generalized interaction matrices, that can be obtained experimentally. For LQG control, we also need to identify the turbulent model, that depends on the turbulent voltages applied on the bench and the measurement noise. These calibrations are quite simple to **perform**.

4.B. AO results

First, we present the results obtained in classic AO on HOMER. We correct the on-axis direction, which corresponds to star 0 on Fig. 2, with the DM52 conjugated with the pupil. All results presented in AO case are obtained with **an** integrator control. **An** LQG control has also been implemented for this configuration, it presents performance **similar to an** integrator control. These results are not presented in this paper, as experimental implementation and comparison of LQG and integrator control laws have been fully studied in AO case in [29].

For **an** integrator control, we compute the control matrix presented in Subsection 3.B: pseudo-inverse of the interaction matrix with a filtering of modes associated with the 6 lowest eigenvalues. The resulting condition number is around 50. We use a constant 0.5 integrator gain. The gain value and the number of truncated modes are tuned to obtain the best performance in direction of star 0. Figure 9 presents long-exposure point spread functions (PSFs) obtained without AO correction in presence of turbulence (Fig. 9 - left) and long-exposure PSFs in closed-loop (Fig. 9 - right). The open-loop SR without correction is about 7% for each star in the FoV. The performance obtained in AO are described in Table 2. When performing AO correction, we obtain a SR of 66% on star 0, that corresponds to both WFS and correction directions. On the border of the FoV, we measure a SR of 12% due to the anisoplanatism effect. We recall that the on-axis internal SR is also 66% for this experiment due to the **numerical rounding of the SR linked to the uncertainties of the measurement.** Let us now compare experimental and numerical results obtained with the end-to-end simulation of HOMER bench. Figure 10 presents the SR obtained on different stars in the FoV within experiments (dashed line) and simulations (solid line). This comparison takes into account the scaling of numerical SRs by measured internal SRs, as explained in Subsection 4.A.1. The experimental and numerical curves are in great agreement. This confirms that we have a good numerical simulation of HOMER bench in AO and also a good modeling of its components. We can notice on Fig. 10 that the experimental results

are slightly better for the stars on the border of the FoV. It is probably due to an error of the experimental position of the border stars or to an evolution of the internal SR of these stars during measurements.

4.C. Experimental results for MCAO control

We focus now on the implementation of MCAO concept using integrator or LQG control. In the following, the WFS directions are given by stars 3, 6 and 10 on Fig. 2. We first describe the results obtained in this configuration and then the tuning of both control laws.

4.C.1. Comparison between integrator and LQG control laws

The results presented here are the first experimental results obtained with LQG control in MCAO. We compare in the following the performance obtained in the FoV with **an** integrator control, described in Subsection 3.B, and **a** LQG control, described in Subsection 3.C. Tuning of LQG and integrator controls are described and discussed respectively in Subsections 4.C.2 and 4.C.3. Note that all the matrices used for control computation are those identified in Subsection 4.A.3. Table 3 presents the SR obtained in 4 directions of the FoV for both control laws: star 0 in the center of the FoV, which is not seen by the WFSs, and the WFS directions stars 3, 6 and 10. We also give the SR obtained with the end-to-end simulation of HOMER, scaled by the internal SR measured for each star. Note that the SR obtained with **a** LQG control is the same as the internal SR due to the **numerical rounding** and the precision of the SR measurements. As **an** integrator control naturally reconstructs the phase in the DM space, the results obtained in MCAO with an integrator control are very good: we obtained 53% of SR averaged in the FoV (see Subsection 3.B). LQG control gives a better performance with a higher SR on all measured directions of interest and **on** average with 56% of SR in the FoV (Table 3). These results give a successful demonstration of the applicability of LQG control on a real MCAO system despite inevitable uncertainties on system models and experimental conditions. The case presented here validates the LQG controlled MCAO configuration, with the advantage of a structurally stable control law. Figure 11 shows the

performance of the MCAO correction with LQG control compared to the AO case. We can see that MCAO correction is very efficient in the whole FoV. As shown on Figure 12 - right, the principal limitation of the MCAO performance in our test is mainly due to the NCPA that are not corrected for the moment. The SR map presented here is very similar to the one presented on Fig. 8. We also present the map of the SR obtained in AO on Figure 12 - left for comparison.

For this first experimental implementation of LQG control on a MCAO system, we generate and thus estimate the turbulence in the DM space, which simplifies the calibration procedure. This configuration is very favorable to integrator control that reconstructs implicitly the turbulence in the DM space. The integrator control has very good performance because it corrects almost all the turbulence generated by the DMs. In a situation where the generation of the turbulent phase would be in a different space than the DM's, the gain in performance for LQG control should be even higher, due to the prediction and spatial aliasing capabilities of the Kalman filter. [29] has demonstrated the ability of LQG control to correct the turbulence generated by a phase screen in off-axis direction despite inevitable model errors in experiments. The implementation of LQG control to correct turbulence generated by phase screens in MCAO requires to adapt the calibration procedure for the identification of LQG control models. In a realistic turbulence case, **a** LQG control in MCAO will give better and more homogeneous performance in the FoV compared to **an** integrator control, as shown in [29] with numerical simulations.

4.C.2. Best tuning of LQG control in experimental MCAO case

The measurement noise variance σ_w^2 is a parameter that allows to tune the performance of the LQG control. Its effect is studied here experimentally and in simulation. Figure 13 shows the mean performance in the FoV obtained in MCAO configuration as a function of σ_w^2 used in the LQG gain computation in Eq. (25). We recall that $\Sigma_w = \sigma_w^2 \mathbf{I}$. In simulation, the WFS noise is set to $\sigma_w^2 = 5 \times 10^{-4}$ pixels^2 which is its estimated value from the slope data. The LQG control is not highly sensitive to the choice of σ_w^2. In experimental tests, the best noise

variance, leading to highest performance, is systematically higher than the measured one. Its value has been set to $\sigma_w^2 = 5 \times 10^{-3}$ pixels^2. One could naively expect that the best performance would be obtained with a Kalman gain computed with a noise variance close to the measured WFS noise level. In fact, the issue here is the relative level of modeling error between measurement and state transition equations of the Kalman filter. A higher value of σ_w^2 will result in a lower value of the Kalman gain: errors affect the measurement model in a way that leads to an increased measurement error variance, so that increasing σ_w^2 results in better performance. In our experiment, the best performance **is** obtained with values of σ_w^2 slightly higher than the measured value. This suggests that modeling errors affect more the measurement model. We have compared experimental results with numerical simulations of HOMER bench, where much less models errors are present, so that the performance is kept high for low values of σ_w^2. The good matching found between both performance suggests that models errors can be partly offset by the tuning of σ_w^2. The performance is not very sensitive to this parameter but an over-estimation is to be preferred to account for inevitable errors in the measurement model.

4.C.3. Tuning of the integrator control in MCAO

We now optimize the performance obtained in the whole FoV with **an** integrator control described in Subsection 3.B. For both experimental and numerical results, the integrator gain is set to 0.5 because it leads to the best performance and it ensures stability. The control matrix is obtained as a truncated generalized inverse of the generalized interaction matrix. To ensure a condition number of 500, 20 modes are filtered out in the TSVD. This control law is dependent on the directions of WFS and no explicit optimization of the correction in other direction is possible. A way to optimize integrator control performance is to choose the truncated threshold. Figure 14 presents the **mean** SR in the FoV obtained with **an** integrator control as a function of the number of truncated modes in the TSVD. We notice that experimental and numerical results are in good agreement. Similar results have been obtained with lower gains. In simulation, we can see that the performance is the same for 0

to 20 truncated modes. In experiments, with too few modes truncated, waffle modes appear and severely limit performance. This is probably due to bad seen modes that are not fully filtered in the TSVD and to the quality of the interaction matrix.

4.D. Experimental results for TAO

In this section, we present the first experimental results obtained in closed-loop in TAO. The interest of using **a** LQG control is great in this case because it performs a reconstruction and a prediction of the turbulent volume in real time making an optimal use of residual WFS data. It then **allows projection of the** turbulence in a specific direction to obtain optimal DM correction. The performance obtained in TAO in one direction can be compared with results obtained in the same direction with AO correction. In fact, TAO **allows correction** in a direction where there is no bright star for WFS. In LTAO, when several LGS are used for WFS, this approach also allows to partially solve the cone effect. **Moreover**, we show the performance obtained in GLAO with **an** integrator control. Classic controllers, such as least-square plus integrator, are dedicated to zeroing the slopes measurements in the directions of WFSs. Thus a particular field of correction cannot be specified. A classic integral controller, such as the GLAO control described in Subsection 3.B, provides an average correction in the FoV.

For this experiment, the turbulence is analyzed in three directions (stars 3, 6 and 10) and then the correction is applied with one DM conjugated to the entrance pupil. **A** LQG control has been implemented with **the** matrices described in Subsection 4.A.3. We choose the direction of star 0 as the optimization correction for TAO. As already shown in Subsection 4.C.2, it is possible to modify LQG performance by tuning the noise variance σ_w^2. Figure 15 shows the dependence of SR performance in the optimized direction as a function of σ_w^2 in the LQG gain in Eq. (25). For experimental results, the best noise variance that leads to the highest performance is higher than the measured one, that is $\sigma_w^2 = 5 \times 10^{-2}$ pixels^2 for a measured value of 5×10^{-4} pixels^2. We see a maximum of the performance in experimental

results whereas the simulation performance is rather constant for low values of σ_w^2 and decreases with higher ones. These results are similar to those presented in Subsection 4.C.2 and have the same explanation. We have to increase the value of σ_w^2 to take into account model errors. GLAO integrator control has been computed with a generalized control matrix with 6 modes filtered out and a gain of 0.5. **This control has been optimized as in Subsection 4.C.3.**

Table 4 gathers the results obtained in TAO and GLAO. **The** performance in TAO can also be compared with the SR value obtained in presence of turbulence with a classical AO correction in direction of star 0. In GLAO, the SR is uniform but low in the FoV, as expected, with about 20% of SR on each studied star. In TAO, a SR of 55% is reached on star 0, which is closed to the performance of 60% of SR obtained in AO in the same direction. The difference is due to the residual tomographic error. TAO optimizes the correction on axis, using a single DM. Consequently the correction deteriorates in the FoV in the same manner as in classic on-axis AO, due to anisoplanatism. ***On*** the contrary, MCAO optimizes the correction in the whole FoV thanks to multiple DMs. Note that these experiments have not been performed during the same period as the MCAO ones, which explains why the SR in AO is lower here. LQG TAO control provides an efficient tomographic reconstruction of the turbulent volume, where there is no bright star to perform the WF sensing.

5. Conclusion

This paper is focused on the validation of LQG control for WFAO systems and the test of different WFAO concepts on the ONERA WFAO bench "HOMER", presented in this paper. Closed-loop experimental results obtained with the bench for different WFAO configurations are obtained and analyzed. We first focus on calibration aspects for WFAO systems and especially component calibration and identification of state-space models, that define the LQG control law. We demonstrate that LQG control can be implemented on a real system, and **we** evaluate its performance in MCAO and TAO configurations. This first ***sets***

of experiments show that MCAO performs a good correction in an extended FoV beyond the isoplanatic path and produces better correction than GLAO. TAO allows to correct the turbulence in a specific direction, thanks to a tomographic reconstruction and **a** prediction of the turbulent volume. With the same technical support but an integral controller, GLAO just corrects the turbulence ***on*** average in the FoV with a rather uniform but low performance. We also compare the performance of **an** integrator and **a** LQG control in these different configurations, with a better performance for LQG control. We have chosen to generate the turbulence by the DMs which has several advantages. It ***provides*** more controlled conditions and **simplifies** calibration and LQG model identification. In TAO configuration, the results obtained are of great interest because they show the significant gain in performance brought by LQG control, which allows ***specification of the*** field of correction and **tomographic reconstruction** in real time in closed-loop conditions. Robustness issues have not been addressed in this paper and would deserve specific developments. We have shown however that **a** LQG control can be applied to a complex AO configuration in experimental conditions. The performance robustness is at this stage sufficient to be compatible with practical implementations. All results obtained in this paper are in accordance with numerical results obtained in end-to-end simulations of HOMER bench. This allows ***extension of*** the simulation ***to*** other new configurations as a reliable basis for the preparation of future **set of experiments**.

The results obtained here represent a first step in the frame of the study of VLT/ELT instruments and particularly for tomographic control laws in closed-loop. Also, thanks to the flexibility of HOMER bench configuration, future work shall include comparison with sub-optimal control policies in WFAO, e.g. closed-loop MMSE control or POLC, *etc.* Different turbulent conditions shall also be explored particularly in presence of high order effects that are likely to destabilize the optimal modal gain integrator approach in MCAO, as shown in [41]. To realize such conditions, a turbulence generator is planned to be used. It will be more representative of spatial and temporal characteristics of the turbulence, leading to more

realistic and rich perturbations. Their impact on performance for different control laws should hence lead to interesting results. Concerning the new WFAO concepts, HOMER's flexibility allows an easy change of GSs number and configuration, together with the corrected FoV. However, more complex atmospheric effects such as mis-conjugation between turbulence and DM layers, or LGS effects need to be addressed, together with a study in low SNR conditions.

Developments of HOMER bench are thus ongoing to simulate even more realistic WFAO systems, leading to a useful tool for VLT/ELT instrument studies.

6. Acknowledgments

The authors want to thank B. Fleury, F. Mendez, J. Montri, V. Bentadj-Paris and V. Michau who have participated to the integration of HOMER. We also thank B. Desruelle who has allowed the funding of this bench with the support of the DGA, Ministère de la Défense (contract N. 0534028). We thank Shaktiware, ALPAO and GEPI for their contributions. We also thank G. Rousset for fruitful discussions about MCAO. This work also received the support of PHASE, the high angular resolution partnership between ONERA, Observatoire de Paris, CNRS and Université Paris Diderot. The activities outlined in this paper have been partially funded as part of the European Commission, Seventh Framework Programme (FP7), Capacities Specific Programme, Research Infrastructures; specifically the FP7, Preparing for the Construction of the European Extremely Large Telescope Grant Agreement, Contract number INFRA-2007-2.2.1.28.

References

1. F. Roddier, *Adaptive Optics in astronomy* (Cambridge University Press, 1999).
2. J.-M. Beckers, "Increasing the size of the isoplanatic patch with multi conjugate adaptive optics", in *Proceedings of a ESO Conference on Very Large Telescopes and their Instrumentation*, M.H. Ulrich, ed., (ESO Conference and Workshop Proceedings, 1988), No. 30, 693-703.
3. D. C. Johnston and B. M. Welsh, "Analysis of multiconjugate adaptive optics", J. Opt. Soc. Am. A **11**, 394-408 (1994).
4. L. Gilles and B. L. Ellerbroek, "Split atmospheric tomography using laser and natural guide star", J. Opt. Soc. Am. A **25** (2008)
5. F. Rigaut, "Ground-Conjugate wide field adaptive optics for the ELTs", in *ESO Conference and Workshop Proceedings*, E. Vernet, R. Ragazzoni, S. Esposito, and N. Hubin, eds. (Garching, Germany, ESO, 2002), No. 58, p. 11.
6. N. Hubin, R. Arsenault, R. Conzelmann, B. Delabre, M. Le Louarn, S. Stroebele and R. Stuik, "Ground Layer Adaptive Optics", *Comptes Rendus de l'Académie des Sciences Physique* **6**, pp. 1099-1109 (2005).
7. E. Gendron, F. Assémat, F. Hammer, P. Jagourel, F. Chemla, P. Laporte, M. Puech, M. Marteaud, F. Zamkotsian, A. Liotard, J.-M. Conan J.-M., T. Fusco and N. Hubin, "FALCON: multi-object AO", *Comptes Rendus de l'Académie des Sciences Physique* **6**, pp 1110-1117 (2005).
8. E. P. Wallner, "Optimal wave-front correction using slope measurements", J. Opt. Soc. Am. A **73**, 1771-1776 (1983).
9. T. Fusco, J.-M. Conan, G. Rousset, L. M. Mugnier and V. Michau, "Optimal wavefront reconstruction strategies for Multiconjugate Adaptive Optics", J. Opt. Soc. Am. A **18**, 2527-2538 (2001).
10. R. N. Paschall, M. A. Von Bokern and B. M. Welsh, "Design of a linear quadratic Gaussian controller for an adaptive optics system",*IEEE Conference on Decision and*

Control (IEEE, 1991), Vol. 2, pp 1761-1769

11. R. Paschall and D. Anderson, "Linear Quadratic Gaussian control of a deformable mirror adaptive optics system with time-delayed measurements", Appl. Opt. **32**, 6347-6358 (1993).
12. D. Looze, M. Kasper, S. Hippler, O. Beker and R. Weiss, "Optimal compensation and implementation for adaptive optics systems", ESA Bull. **15**, pp. 97-88 (2003).
13. D. Wiberg, C. Max and D. T. Gavel, "A spatial non-dynamic LQG controller: Part I, Application to adaptive optics", *IEEE Conference on Decision and Control* (IEEE, 2004), Vol. 3, pp 3326-3332
14. B. Le Roux, J.-M. Conan, C. Kulcsár, H.-F. Raynaud, L. M. Mugnier and T. Fusco, "Optimal control law for classical and Multiconjugate Adaptive Optics", J. Opt. Soc. Am. A **21**, 1261-1276 (2004).
15. C. Kulcsár, H.-F. Raynaud, C. Petit, J.-M. Conan and P. Viaris de Lesegno, "Optimal control, observers and integrators in adaptive optics", Opt. Express **14**, 7464-7476 (2006).
16. C. Petit, J.-M. Conan, C. Kulcsár, H.-F. Raynaud, T. Fusco, J. Montri and D. Rabaud, "Optimal Control for Multi-conjugate Adaptive Optics", *Comptes Rendus de l'Académie des Sciences Physique* **6**, pp 1059-1069 (2005).
17. B. Ellerbroek and C. Vogel, "Simulations of closed-loop wavefront reconstruction for multiconjugate adaptive optics on giant telescopes", Proc. SPIE **5169-23**, pp 206-17 (2003)
18. L. Gilles, "Closed-loop stability and performance analysis of least-squares and minimum variance control algorithms for multi-conjugate adaptive optics", Appl. Opt. **44**, 993-1002 (2005).
19. P. Piatrou and L. Gilles, "Robustness study of the pseudo open-loop controller for multiconjugate adaptive optics", Appl. Opt. **44**, 1003-1010 (2005).
20. C. Béchet, M. Tallon and E. Thiébaut, "FRIM: minimum-variance reconstructor with a

fractal iterative method", Proc. SPIE **6272**, 62722U (2006)

21. E. Marchetti, R. Brast, B. Delabre, R. Donaldson, E. Fedrigo, C. Frank, N. Hubin, J. Kolb, M. Le Louarn, J.-L. Lizon, S. Oberti, F. Quirós-Pacheco, R. Reiss, J. Santos, S. Tordo, E. Vernet, R. Ragazzoni, C. Arcidiacono, P. Bagnara, A. Baruffolo, E. Diolaiti, J. Farinato and M. Lombini, "MAD: Practical implementation of MCAO concepts", *Comptes Rendus de l'Académie des Sciences Physique* **6**, pp 1118-1128 (2005)
22. E. Marchetti, R. Brast, B. Delabre, R. Donaldson, E. Fedrigo, C. Frank, N. Hubin, J. Kolb, J.-L. Lizon, M. Marchesi, S. Oberti, R. Reiss, C. Soenke, S. Tordo, A. Baruffolo, P. Babnara, A. Amorim and J. Lima, "MAD on sky results in star oriented mode", Proc. SPIE, **7015**, 14 (2008)
23. M. Lloyd-Hart, C. Baranec, N. Mark Nilton, M. Snyder, T. Stalcup and J. R. P. Angel, "Experimental results of ground-layer and tomographic wavefront reconstruction from multiple laser guide stars", Opt. Express **14**, 7541-7551 (2006)
24. M. Bec, F. Rigaut, R. Galvez, G. Arriagada, M. Boccas, G. Gausachs, D. Gratadour, E. James, R. Rojas, R. Rogers, M. P. Sheehan, G. Trancho and T. Vucina, "The Gemini MCAO bench: system overview and lab integration", Proc. SPIE **7015**, 228 (2008)
25. E. Laag, M. Ammons, T. Gavel and R. Kupke, "Multiconjugate adaptive optics results from the laboratory for adaptive optics MCAO/MOAO testbed", J. Opt. Soc. Am. A **25**, 2114-2121 (2008)
26. S. Mark Ammons, L. Johnson, E. A. Laag, R. Kupke, D.T. Gavel, B. J. Bauman and C. E. Max, "First laboratory demonstration of multi-object and laser tomography adaptive optics on a 10 meter telescope", PASP, 2009, To be published (arXiv/0901.1716)
27. C. Petit, J.-M. Conan, C. Kulcsár, H.-F. Raynaud, T. Fusco, J. Montri, F. Chemla and D. Rabaud, "Off-Axis Adaptive Optics with Optimal Control: Experimental and Numerical Validation", Proc. SPIE **5903** (2005)
28. K. Hinnen, M. Verhaegen and N. Doelman, "Exploiting the spatio-temporal correlation in adaptive optics using data-driven H2-optimal control", J. Opt. Soc. Am. A **24**, 1714-

1725 (2007)

29. C. Petit, J.-M. Conan, C. Kulcsár and H.-F. Raynaud, "LQG control for AO and MCAO: experimental and numerical analysis", J. Opt. Soc. Am. A **26**, 1307-1325 (2009).
30. D. P. Looze, "Discrete-time model of an adaptive optics system," J. Opt. Soc. Am. A **24**, No. 9, 2850–2862 (2007).
31. C. Correia, H.-F. Raynaud, C. Kulcsár and J.-M. Conan, "Globally optimal minimum mean-square error control in adaptive optical systems with mirror dynamics", Proc. SPIE **7015**, 50 (2008)
32. W. Gaessler, C. Arcidiacono, S. Egner, T. M. Herbst, D. Andersen, H. Baumeister, P. Bizenberger, H. Boehnhardt, F. Briegel, M. Kuerster, W. Laun, L. Mohr, B. Grimm, H.-W. Rix, R.-R. Rohloff, R. Soci, C. Storz, W. Xu, R. Ragazzoni, P. Salinari, E. Diolaiti, J. Farinato, M. Carbillet, L. Schreiber, A. Eckart, T. Bertram, C. Straumbmeier, Y. Wang, L. Zealounk, G. Weigelt, U. Beckmann, J. Behrend, T. Driebe, M. Heininger, K.-H. Hofmann, E. Nussbaum, D. Schertel and E. Masciadri, "LINC-NIRVANA: MCAO toward extremely large telescopes", *Comptes Rendus de l'Académie des Sciences Physique* **6**, pp 1129-1138 (2005)
33. V. Tatarski, "Wave propagation in a turbulent medium", (Dover Publication, Inc. New York, 1961)
34. H.-F. Raynaud, C. Kulcsár, C. Correia, J.-M. Conan, "Multirate LQG AO control", Proc. SPIE **7015**, 115 (2008)
35. P. Joseph and J. Tou, "On linear control theory", AIEE Trans. on Appl. and Indus **80**, pp 193-196 (1961)
36. P. Whittle, *Optimization over time – Dynamic programming and stochastic control* (John Wiley & sons, 1982).
37. D. Looze, O. Beker, M. Kasper and S. Hippler, "Optimal compensation and implementation for adaptive optics systems", *IEEE Conference on Decision and Control* (IEEE, 1999), Vol. 2, pp 1715-1720.

38. D. Looze, "Minimum variance control structure for adaptive optics systems", J. Opt. Soc. Am. A **23**, pp 603-612 (2006)

39. J.-F. Sauvage, T. Fusco, G. Rousset and C. Petit, "Calibration and pre-compensation of non-common path aberrations for extreme adaptive optics", J. Opt. Soc. Am. A **24**, 2334-2346 (2007)

40. J. Kolb, "Eliminating the static aberrations in an MCAO system", Proc. SPIE **6272**, 122, (2006)

41. F. Quirós-Pacheco, "Reconstruction and Control Laws for Multi-Conjugate Adaptive Optics in Astronomy", PhD thesis, Imperial College, London, 2006. `http://optics.nuigalway.ie/theses/FernandoQuiros_PhDthesis.pdf`

List of Figure Captions

- Fig. 1: HOMER bench and its main components.
- Fig. 2: GSs configurations (solid boxes for WFAO and dashed boxes for AO) and science star constellation (crosses).
- Fig. 3: Relative separation $\delta = \alpha h/D$ between two stars in the FoV for a layer at altitude h. We see the footprint of the pupil in altitude and their separation.
- Fig. 4: Sketch of a constant envelope collimator. The marginal ray passing the edge of the pupil in the collimated entry space, corresponding to the extreme half-field, passes through the primary focal point of the lens. It allows to change the GS footprint size with the altitude whereas the meta-pupil keeps its original size. We see on the bottom the footprint for two positions of the DM88: on the left it corresponds to $\delta = 100\%$ and on the right to $\delta = 0\%$
- Fig. 5: WFS display: on top, full display with all 7×7 sub-apertures. Bottom-right, zoom on one sub-aperture: dashed squares represent the windows cut by the RTC for WF sensing on each GS.
- Fig. 6: Example of a WFAO system. Turbulence is composed of n_ℓ layers and analyzed thanks to n_{gs} WFSs in the n_{gs} GSs' directions. Correction is performed by n_m DMs, conjugated with $n_m = 2$ altitudes in this picture.
- Fig. 7: Temporal diagram of the system process.
- Fig. 8: Map of internal SR in AO case (left) and MCAO case (right). The standard deviation is 5.8% in AO and 5.6% in MCAO.
- Fig. 9: Left: map of experimental long-exposure PSFs obtained on HOMER without any correction of the turbulence. Right: map of experimental long-exposure PSFs obtained in AO with **an** integrator control. The star surrounded by the dashed square is

altogether WFS and correction direction. The PSFs have been cut off from the original image and artificially brought closer.

- Fig. 10: Comparison of experimental (dashed line) and numerical (solid line) SR in AO with **an** integrator control, according to the footprint relative separation of the stars in the FoV. Note that star with $\delta = 0$ is altogether the WFS and correction direction.

- Fig. 11: Left: map of experimental long-exposure PSFs obtained in AO with **an** integrator control. Right: map of experimental long-exposure PSFs obtained in MCAO with LQG control. The GSs for MCAO are surrounded by a red solid square and for AO by a blue dashed square.

- Fig. 12: Left: map of experimental SR obtained in AO with **an** integrator control. Right: map of experimental SR obtained in MCAO with LQG control. Note that both images are not represented with the same color scale.

- Fig. 13: Comparison of experimental (dashed line) and numerical (solid line) **mean** SR measured in the whole FoV in MCAO, as a function of the noise variance σ_w^2.

- Fig. 14: Comparison of experimental and numerical **mean** SR in the FoV obtained with integrator control as a function of the number of truncated modes in the TSVD of the interaction matrix.

- Fig. 15: Comparison of experimental (dashed line) and numerical (solid line) SR in the direction of optimization in TAO configuration, as a function of the noise variance σ_w^2.

List of Table Captions

- Tab. 1: Size of the interaction matrices for AO, GLAO and MCAO in HOMER case (in this case $n_{gs} = 3$ and $n_m = 2$).

- Tab. 2: SR obtained in AO with **an** integrator control: comparison of experimental (exp) and numerical (sim) SR. We also give the internal SR measured in AO without turbulence. We consider the performance on 4 stars in the FoV: the 3 WFS GSs in MCAO and star 0, the GS in AO in the center of the FoV.

- Tab. 3: Comparison of experimental (exp) and numerical (sim) SR in MCAO with integrator and LQG control. We consider the performance on 4 stars in the FoV: the 3 WFS GSs and star 0 in the center of the FoV.

- Tab. 4: SR obtained on different stars in classical AO in presence of turbulence, in TAO with **a** LQG control and in GLAO with **an** integrator control.

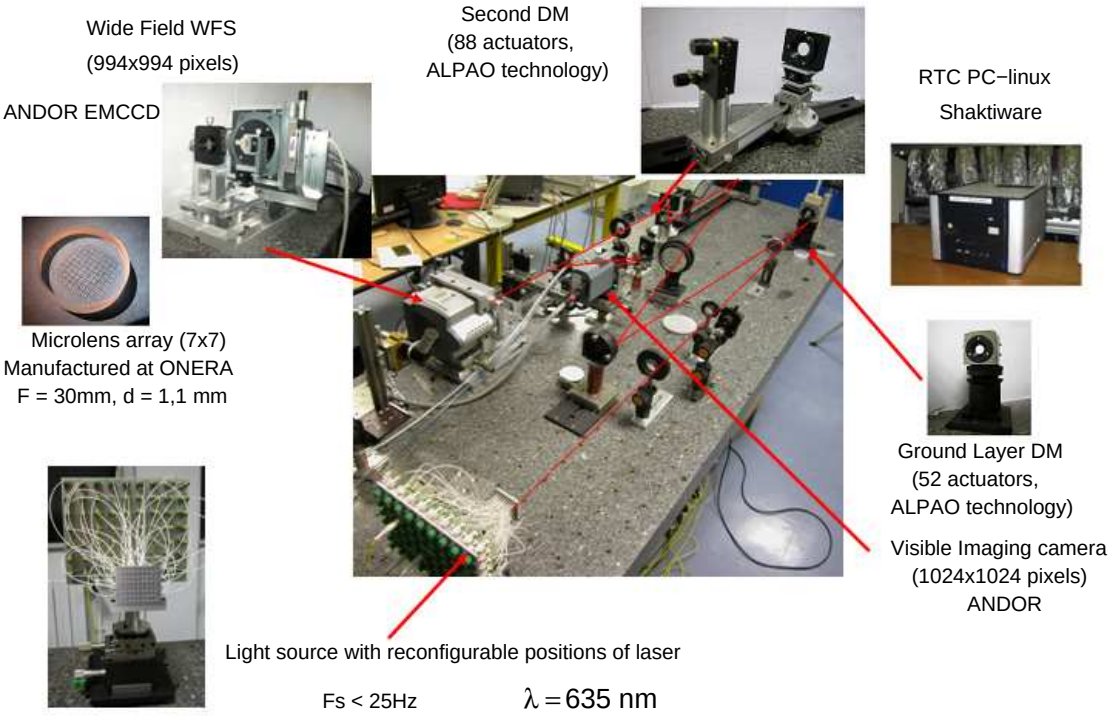

Fig. 1. HOMER bench and its main components.

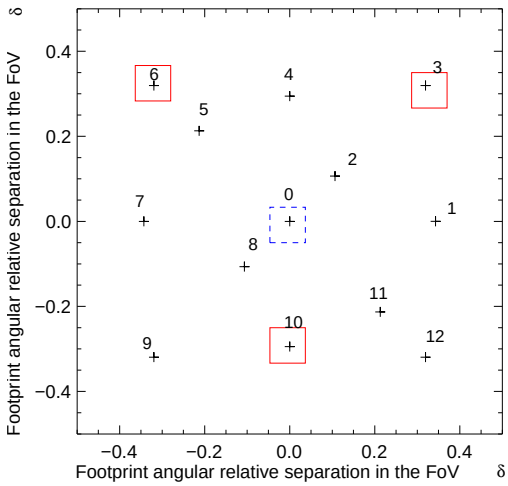

Fig. 2. GSs configurations (solid boxes for WFAO and dashed boxes for AO) and science star constellation (crosses).

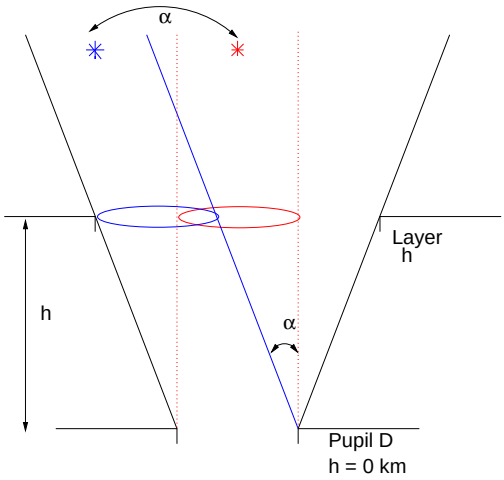

Fig. 3. Relative separation $\delta = \alpha h/D$ between two stars in the FoV for a layer at altitude h. We see the footprint of the pupil in altitude and their separation.

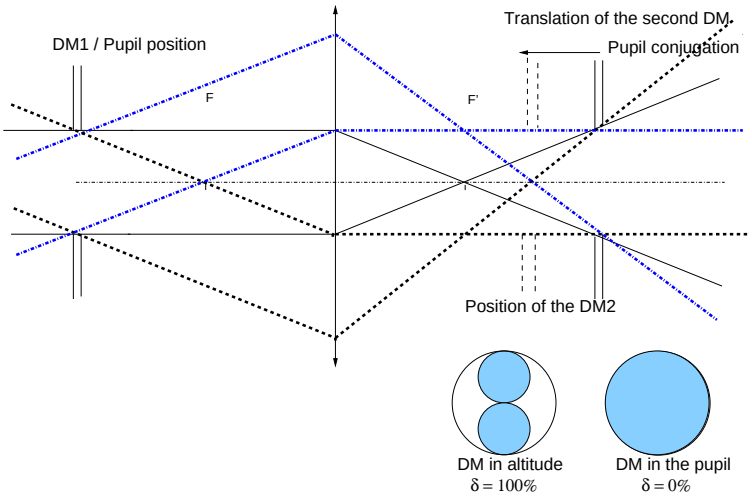

Fig. 4. Sketch of a constant envelope collimator. The marginal ray passing the edge of the pupil in the collimated entry space, corresponding to the extreme half-field, passes through the primary focal point of the lens. It allows to change the GS footprint size with the altitude whereas the meta-pupil keeps its original size. We see on the bottom the footprint for two positions of the DM88: on the left it corresponds to $\delta = 100\%$ and on the right to $\delta = 0\%$

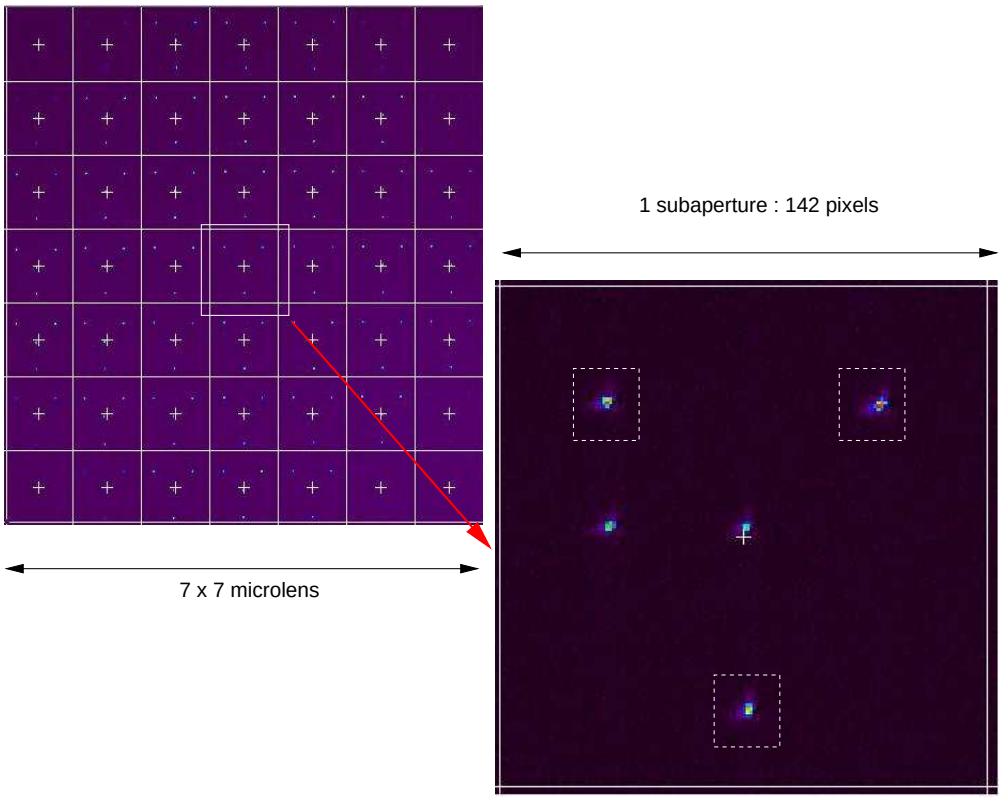

Fig. 5. WFS display: on top, full display with all 7×7 sub-apertures. Bottom-right, zoom on one sub-aperture: dashed squares represent the windows cut by the RTC for WF sensing on each GS.

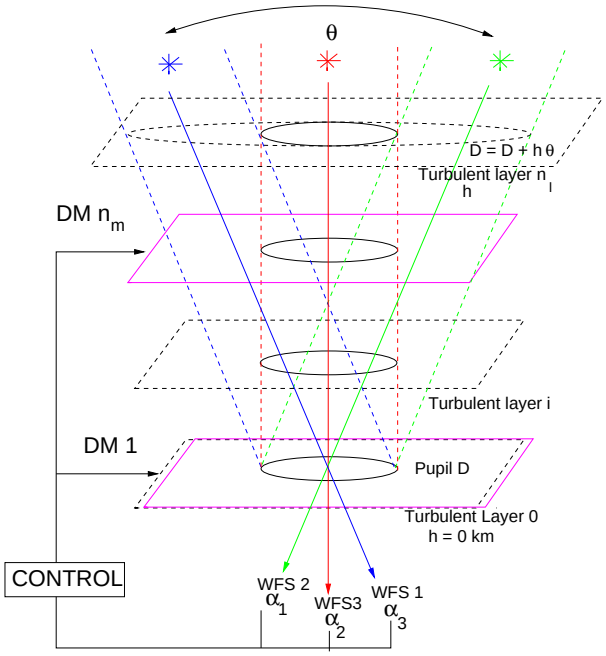

Fig. 6. Example of a WFAO system. Turbulence is composed of n_ℓ layers and analyzed thanks to n_{gs} WFSs in the n_{gs} GSs' directions. Correction is performed by n_m DMs, conjugated with $n_m = 2$ altitudes in this picture.

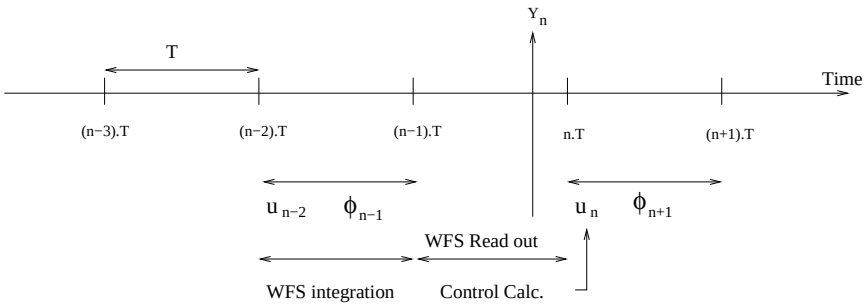

Fig. 7. Temporal diagram of the system process.

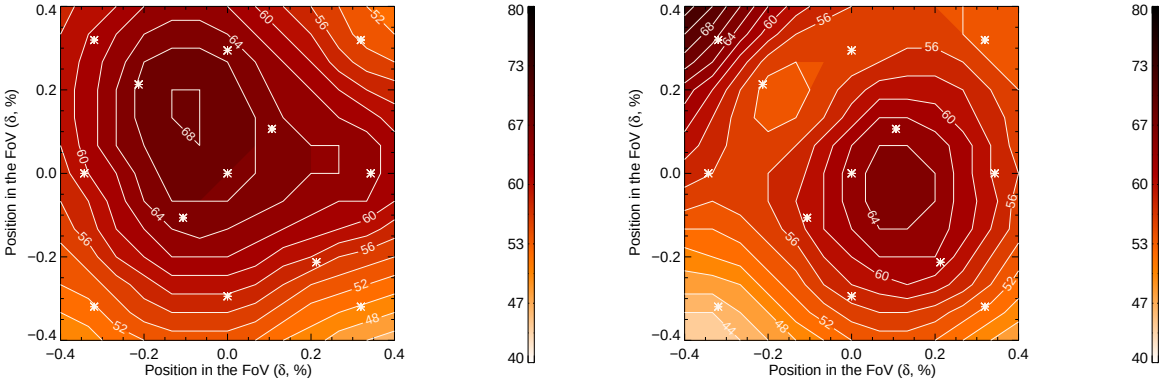

Fig. 8. Map of internal SR in AO case (left) and MCAO case (right). The standard deviation is 5.8% in AO and 5.6% in MCAO.

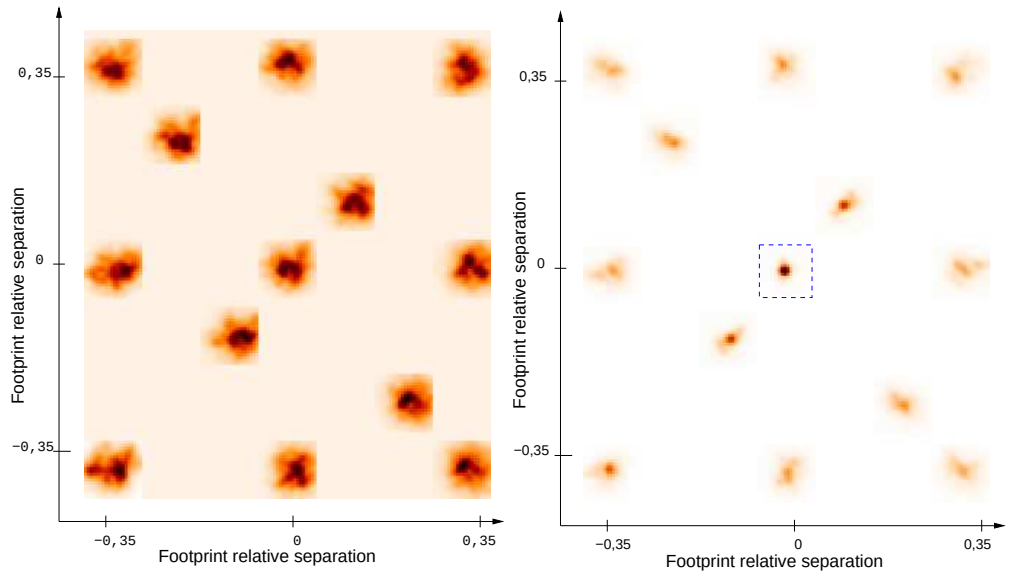

Fig. 9. Left: map of experimental long-exposure PSFs obtained on HOMER without any correction of the turbulence. Right: map of experimental long-exposure PSFs obtained in AO with **an** integrator control. The star surrounded by the dashed square is altogether WFS and correction direction. The PSFs have been cut off from the original image and artificially brought closer.

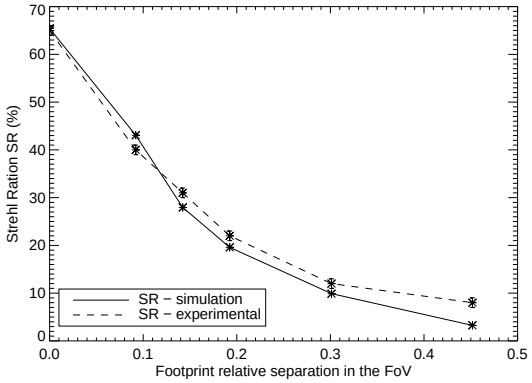

Fig. 10. Comparison of experimental (dashed line) and numerical (solid line) SR in AO with **an** integrator control, according to the footprint relative separation of the stars in the FoV. Note that star with $\delta = 0$ is altogether the WFS and correction direction.

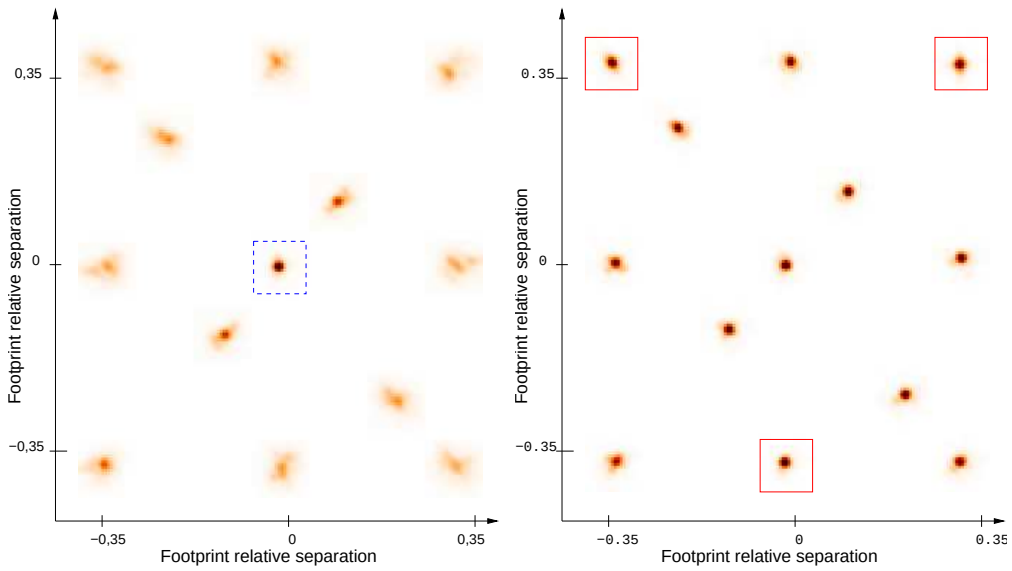

Fig. 11. Left: map of experimental long-exposure PSFs obtained in AO with **an** integrator control. Right: map of experimental long-exposure PSFs obtained in MCAO with **a** LQG control. The GSs for MCAO are surrounded by a red solid square and for AO by a blue dashed square.

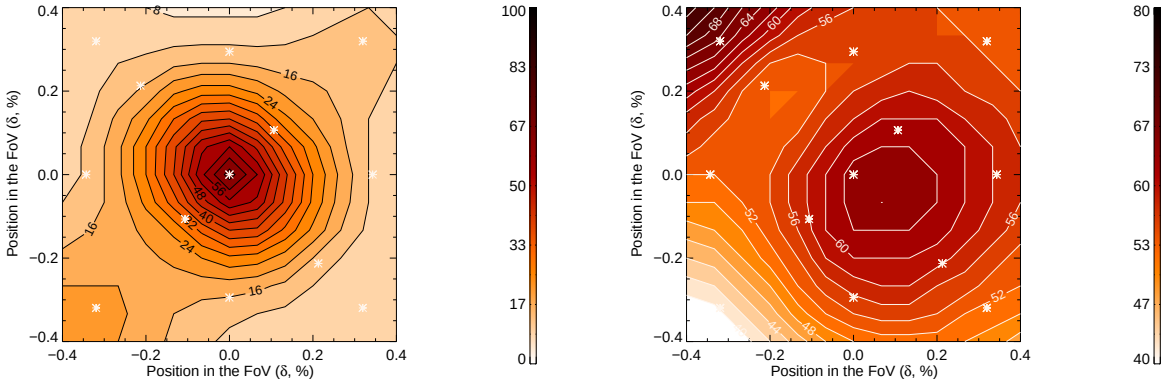

Fig. 12. Left: map of experimental SR obtained in AO with **an** integrator control. Right: map of experimental SR obtained in MCAO with **a** LQG control. Note that both images are not represented with the same color scale.

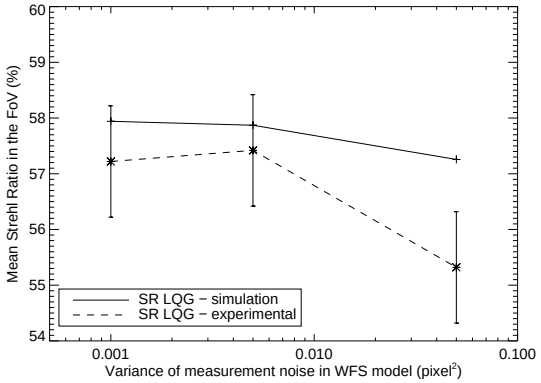

Fig. 13. Comparison of experimental (dashed line) and numerical (solid line) **mean** SR measured in the whole FoV in MCAO, as a function of the noise variance σ_w^2.

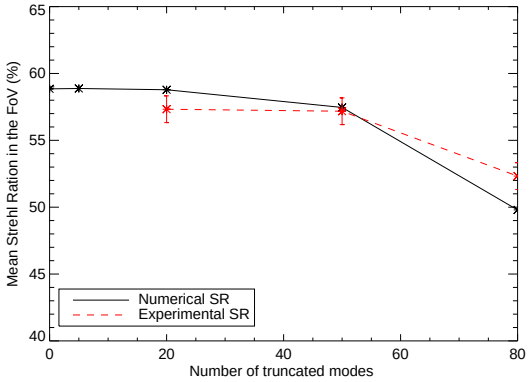

Fig. 14. Comparison of experimental and numerical **mean** SR in the FoV obtained with **an** integrator control as a function of the number of truncated modes in the TSVD of the interaction matrix.

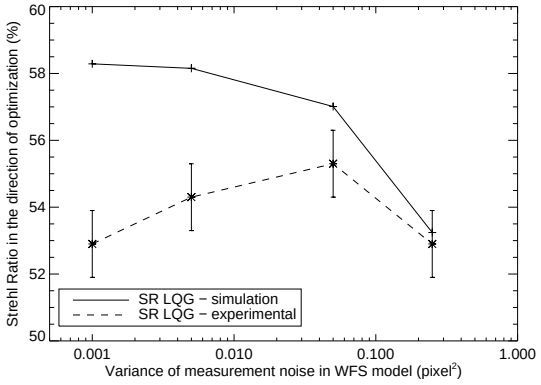

Fig. 15. Comparison of experimental (dashed line) and numerical (solid line) SR in the direction of optimization in TAO configuration, as a function of the noise variance σ_w^2.

Tables

Table 1. Size of the interaction matrices for AO, GLAO and MCAO in HOMER case (in this case $n_{gs} = 3$ and $n_m = 2$).

$\mathbf{M}_{int}^{1,1}$	$\mathbf{M}_{int}^{n_{gs},1}$	$\mathbf{M}_{int}^{n_{gs},n_m}$
74×52	222×52	222×140

Table 2. SR obtained in AO with **an** integrator control: comparison of experimental (exp) and numerical (sim) SR. We also give the internal SR measured in AO without turbulence. We consider the performance on 4 stars in the FoV: the 3 WFS GSs in MCAO and star 0, the GS in AO in the center of the FoV.

Star number	0	3	6	10
Internal SR (%)	66	60	54	58
SR in AO with integrator control (%) (exp)	66	11	13	15
SR in AO with integrator control (%) (sim)	66	8	5	5

Table 3. Comparison of experimental (exp) and numerical (sim) SR in MCAO with integrator and LQG control. We consider the performance on 4 stars in the FoV: the 3 WFS GSs and star 0 in the center of the FoV.

Star number	0	3	6	10
Internal SR (%)	63	57	54	67
SR in MCAO with integrator control (%) (exp)	60	56	52	61
SR in MCAO with integrator control (%) (sim)	61	56	53	66
SR in MCAO with LQG control (%) (exp)	63	57	54	67
SR in MCAO with LQG control (%) (sim)	62	57	54	67

Table 4. SR obtained on different stars in classical AO in presence of turbulence, in TAO with **a** LQG control and in GLAO with **an** integrator control.

Star number	0	3	6	10
Experimental SR in AO (%)	60	13	12	20
Experimental SR in TAO (%) (LQG)	55	12	10	18
Experimental SR in GLAO (%) (integrator)	17	15	18	21